J Nanopart Res (2024) 26:196
https://doi.org/10.1007/s11051-024-06088-y

RESEARCH

Enhanced solid solubility in hcp Co(Mo) nanoparticles formed via inert gas condensation

S. Dhapola · J. E. Shield

Received: 8 April 2024 / Accepted: 17 July 2024

Abstract Co–Mo alloy clusters with extended solubility of Mo in hcp Co were produced by inert gas condensation (IGC). While the equilibrium solubility of Mo in hexagonal close-packed (hcp) Co is on the order of 1 atomic percent, the non-equilibrium aspects of IGC resulted in ~ 18 atomic percent Mo dissolved in hcp Co. The extended solid solutions and hcp structure were observed across all of the processing conditions, which included variation of sputtering power and aperture size. There was, however, variation of nanoparticle size and magnetic behavior with processing parameters. The Co(Mo) nanoparticles were ferromagnetic at room temperature. Coercivities of the nanoparticles produced with a 2.5-mm aperture were independent of sputtering power and significantly higher than those of the nanoparticles produced with a 7-mm aperture. The coercivities of the nanoparticles produced with a 7-mm aperture were slightly power-dependent. Overall, there appeared to be a relationship between coercivity and nanoparticle size.

Keywords Nanoparticle solid solution alloys · Co-Mo alloy clusters · Synthesis · Sputter deposition · Transmission electron microscopy · Hysteresis behavior · Ferromagnetic · Magnetocrystalline anisotropy

S. Dhapola (✉) · J. E. Shield
Mechanical and Materials Engineering, University of Nebraska-Lincoln, Lincoln, NE 68588, USA
e-mail: sdhapola2@huskers.unl.edu

S. Dhapola · J. E. Shield
Nebraska Center for Materials and Nanoscience, University of Nebraska-Lincoln, Lincoln, NE 68588, USA

Introduction

Magnetic materials are integral for any number of technological applications such as automotive, electronics, and clean energy, and therefore, it is important to develop new magnetic materials [1, 2]. Rare earth–based permanent magnets provide the highest energy products, but because of supply chain issues for rare earth elements, researchers are exploring rare earth–free materials [3]. The challenge is in finding compounds with the appropriate combination of high magnetization, anisotropy, and Curie temperature. There are many candidate materials to supplant rare earth–based materials; Cui et al. [4] provide a nice overview of many of these. Instead of searching for new phases and compounds, another approach is to modify the intrinsic behavior of existing materials. Specifically, while elemental Fe and Co have excellent magnetization and Curie temperature, the magnetocrystalline anisotropy is too low for permanent magnet applications. However, Skomski et al. [5] and Kashyap et al. [6] suggest that dissolving 4d or 5d early transition metals (e.g., Mo or W) into Fe or Co can enhance the magnetocrystalline anisotropy.

Published online: 21 August 2024

However, equilibrium solubility levels are very low. For example, less than 1 atomic percent Mo can dissolve in hexagonal close-packed (hcp) Co under equilibrium conditions.

The challenge, then, is to create extended solid solutions during processing. Rapid solidification, for example, can extend solid solubility through solute trapping [7], though for most systems, the extent is limited. Developing solid solutions in immiscible alloy systems has attracted a considerable attention, particularly in catalytic materials because multi-component systems can facilitate higher selectivity and activity [8]. Chemical routes, such as co-reduction, produced Rh(Cu) solid solution nanoparticles though Rh and Cu are immiscible, which improved the catalytic properties of the system [9]. Similarly, Au and Ru solid solution alloy nanoparticles were synthesized by controlling the reduction kinetics of the metal precursors [10], while Ir(Pd) solid solution nanoparticles were prepared by incipient wetness (co-) impregnation of amorphous silica alumina with Ir and Pd dissolved in toluene [11]. Solid solution Ag-Rh is particularly challenging to produce considering there is liquid-phase immiscibility, though solid solution alloys were produced via chemical reduction [12]. Physical routes using inert gas condensation (IGC) [13] successfully produced solid solution Au(Co) and Fe–Au solid solution alloys [14, 15]. Ferrando et al. [8] provides various examples of solid solution alloys being formed from immiscible systems such as Ni–Ag, Ni–Au, and Fe–Ag. Extended solubility of W in hcp Co was achieved by IGC, with some effect on the magnetic behavior, although large solubility extension was limited to smaller particles as larger particles were observed to phase separate [16, 17].

In this paper, efforts were focused on producing solubility extension in Co–Mo using IGC. The effect of different processing conditions, namely, the power and duration in the nucleation zone, on the nanoparticle size, structure, and magnetic behavior was studied.

Experimental procedure

Nanoparticle fabrication

Co–Mo alloy clusters were produced by inert-gas condensation (IGC). DC magnetron sputtering was used to form the atomic gas from a Co–Mo composite target. The composition of the Co–Mo nanoparticles was set using Mo plugs inset in a Co target. For this investigation, 2 Mo plugs with diameters of 0.25 in were inserted into the "racetrack" of the Co target typical of magnetron sputtering so that ~ 11% of the racetrack was Mo, and considering the relative sputtering yields of Co and Mo [18], the expected composition would be ~ 11 at%. The base pressure of the system was less than 10^{-6} Torr. Argon gas was introduced into the cluster-forming chamber in order to facilitate sputtering of the target. Deposition rates were measured in situ using a quartz crystal thickness monitor. Clusters were produced using sputtering powers of 50, 100, and 150 W and two aperture sizes, 2.5 and 7 mm; note that the aperture separates the nucleation chamber from the deposition chamber. The gas flowrate was held constant at 100 sccm. The nucleation chamber was cooled by water for all experiments.

For magnetic measurements, the Co–Mo clusters were imbedded in a SiO_2 matrix by alternate deposition from the cluster source and an RF source positioned perpendicular to the cluster source in the deposition chamber. Overall thickness of the composite films, which were deposited on a Si substrate, was approximately 30 nm. For scanning/transmission electron microscopy (S/TEM) investigation, the nanoparticles were deposited directly onto graphite support films on a Cu grid. A thin layer of SiO_2 was deposited after cluster deposition to protect the nanoparticles from oxidation. S/TEM was accomplished using a FEI Tecnai Osiris operating at 200 kV. The composition of the nanoparticles was determined by energy-dispersive X-ray spectroscopy (EDS) in TEM mode, using a thicker deposition of nanoparticles (i.e., nanoparticle films) to enhance EDS signal and a broad beam. Chemical maps of individual nanoparticles were acquired using EDS in STEM mode. Image analysis for determining average size of the nanoparticles was accomplished by ImageJ. About ~ 2000 nanoparticles per sample were analyzed. A histogram was plotted, and then fit with a Gaussian to determine mean and standard deviations.

The magnetic measurements were conducted at 300 K using a Quantum Design VersaLab Vibrating Sample Magnetometer with a maximum field of 3 T. The magnetic signal from the diamagnetic

Si substrate was subtracted from the sample signal by fitting a straight line to the high-field region and subtracting the linear portion from the measured signal.

Results and discussion

The nanoparticles produced with the 2.5 mm aperture were, visually, more varied in size and morphology than those produced with the 7-mm aperture, particularly for those processed at 100 and 150 W (Fig. 1). For the latter powers, the larger nanoparticles appear to be non-spherical (Fig. 1b, c). Table 1 shows the sizes determined under all processing conditions. Note the broad size distribution for the nanoparticles produced with a 2.5-mm aperture, as the coefficient of variation ($\sigma/d > 0.27$).

Table 1 Nanoparticle size as a function of processing conditions

Power (W)	Size (nm)@2.5 mm aperture	Size (nm)@7 mm aperture
50	6.0±1.7	16.5±2.3
100	6.3±1.7	14.0±1.5
150	10.7±4.6	13.2±2.3

The nanoparticles produced with an aperture size of 7 mm were more regularly shaped with a spherical morphology and were largely monodispersed (coefficient of variation $\sigma/d < 0.17$ for all three sputtering powers, and close to 0.1 for 50 and 100 W) (Fig. 1d–f; Table 1). For nanoparticles produced at both aperture sizes, there is a slight dependency on sputtering power (Fig. 2). Interestingly, for the

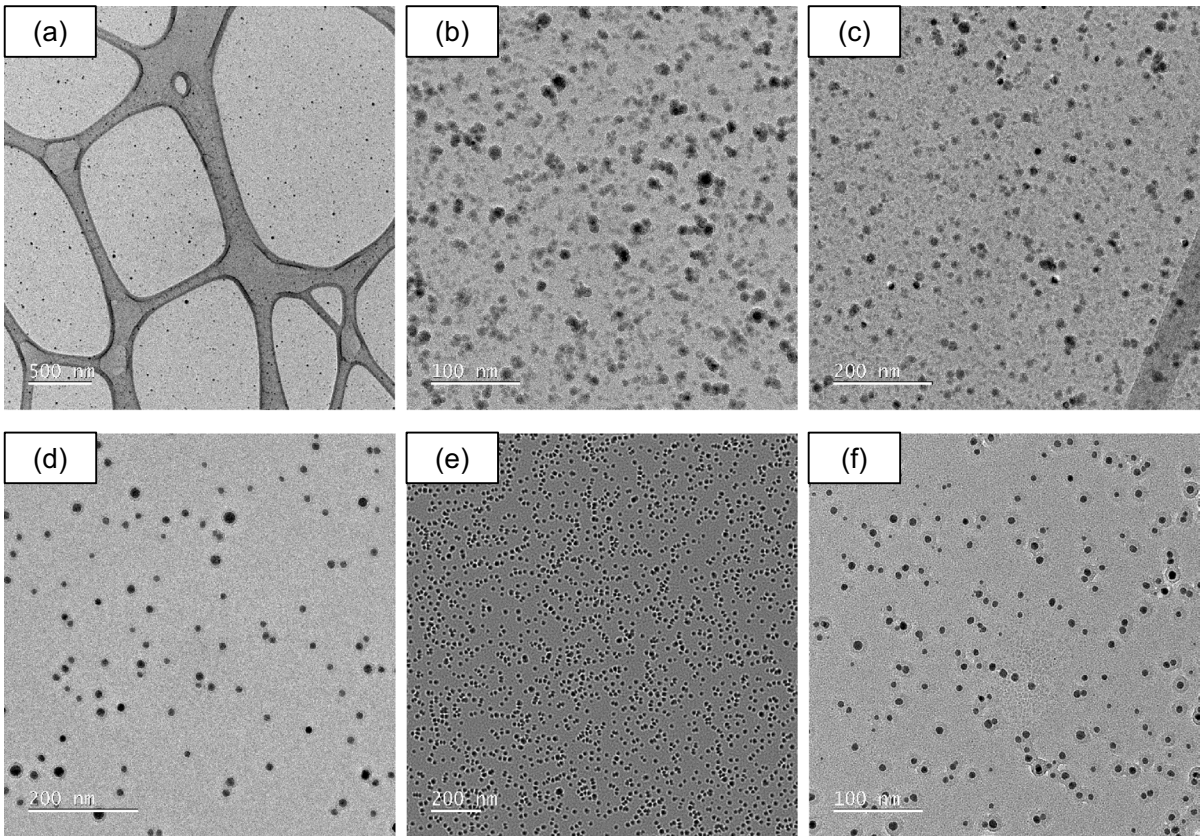

Fig. 1 TEM images of the as-deposited Co(Mo) nanoparticles produced with varied sputtering power (50 W, 100 W, 150 W) and aperture sizes (2.5, 7 mm). For 2.5-mm aperture, nanoparticles produced from different powers are presented in **a** 50 W, **b** 100 W, and **c** 150 W. For 7-mm aperture, nanoparticles produced from different powers are presented in **d** 50 W, **e** 100 W, **f** 150 W

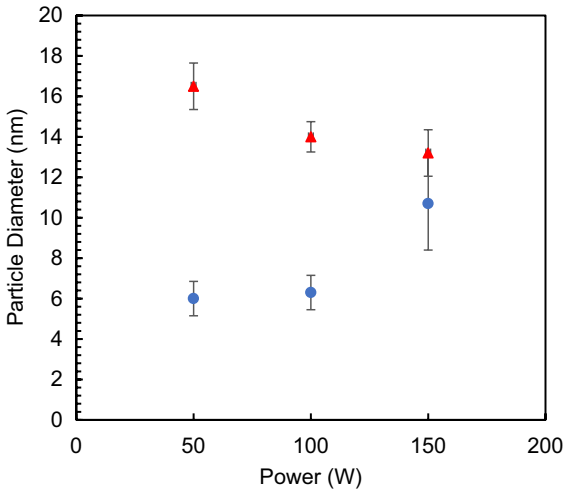

Fig. 2 Nanoparticle diameter as a function of sputtering power for nanoparticles formed with a 2.5-mm aperture (circles) and a 7-mm aperture (triangles)

2.5-mm aperture, the dependency is positive, while for the 7-mm aperture, it is negative (i.e., nanoparticle size decreases with increasing power). This could reflect the dynamics of the nanoparticle formation. With a 2.5-mm aperture, the convection within the nucleation chamber may by more chaotic/turbulent since it is more difficult for the gas to flow through the smaller aperture. This may reduce the dwell time of nanoparticles/nuclei in the nucleation and growth region. The higher power may increase the nucleation zone, enhancing growth. On the other hand, with a 7-mm aperture, less turbulence may exist, enhancing nucleation and growth. The slight decrease in size may be the result of higher atom energies and thus lower "sticking" probabilities, decreasing growth. Further work is necessary to better understand the growth dynamics.

The overall chemical composition and the spatial distribution of the Co and Mo were investigated by EDS. For the overall composition, a thicker deposition of nanoparticles was used to increase x-ray production. A nanoparticle film of approximately 30-nm thickness was used, and EDS analysis was done with a spread-out electron beam in TEM mode. Compositional analysis revealed 82 at% Co and 18 at% Mo. This concentration of Mo was higher than that predicted when considering areal coverage of Mo along the racetrack and the sputtering yields of Co and Mo from [18], suggesting that under the sputtering conditions, here, relatively more Mo is sputtered, increasing the Mo content in the nanoparticles. For the spatial distribution, STEM mode was used to investigate individual nanoparticles. A number of nanoparticles for both aperture sizes (2.5 and 7 mm) were analyzed, and Fig. 2 shows nanoparticle diameter as a function of sputtering power. The high-angle annular dark field (HAADF) STEM image (Fig. 3a, d) showed a relatively even contrast, suggesting compositional homogeneity. The EDS maps (Figs. 3b, c, e, f) confirm this, as both Co and Mo appear to be homogeneously distributed. There is no evidence of a core/shell morphology, as has been observed in other works [19]. The difference between this work and [19] may be due to the different processing conditions under which the nanoparticles were formed, as dynamics of the nucleation and growth would be expected to be sensitive to power, gas flow, and aperture sizes.

HRTEM images revealed that under all conditions, the nanoparticles were crystalline, evidenced by the lattice fringes (Fig. 4). In many cases, lattice fringes extended across the diameter of the nanoparticles, and in other cases, they were more predominantly observed in the center, while a more defected region was observed further out. In general, the structures lacked extensive defects, as the lattice fringes were regular and continuous. Considering the crystalline nature of the nanoparticles and the even distribution of Mo determined from the EDS maps above, it is evident that the nanoparticles are solid solutions, with about 18 at% Mo dissolved into Co.

The fast Fourier transforms (FFT) of the HRTEM images were used to determine the crystal structures. Patterns to definitively determine crystal structures require both cross fringes and zone axes distinguishable from different crystal systems. While such patterns were not observed for every processing condition, crystal structures determined could be used to index fringes from other nanoparticles. From this technique, distinct structures were found for the different aperture sizes, but constant across powers.

For the nanoparticles formed with the 2.5-mm aperture, a nanoparticle formed at 150 W was used to determine the crystal structure (Fig. 5a). Several sets of lattice fringes were evident, resulting in a well-formed FFT (Fig. 5b). This was indexed to the [1213] zone axis of a hexagonal close-packed (hcp) structure, with $a = 2.50$ Å and $c = 5.0$ Å. For the nanoparticle

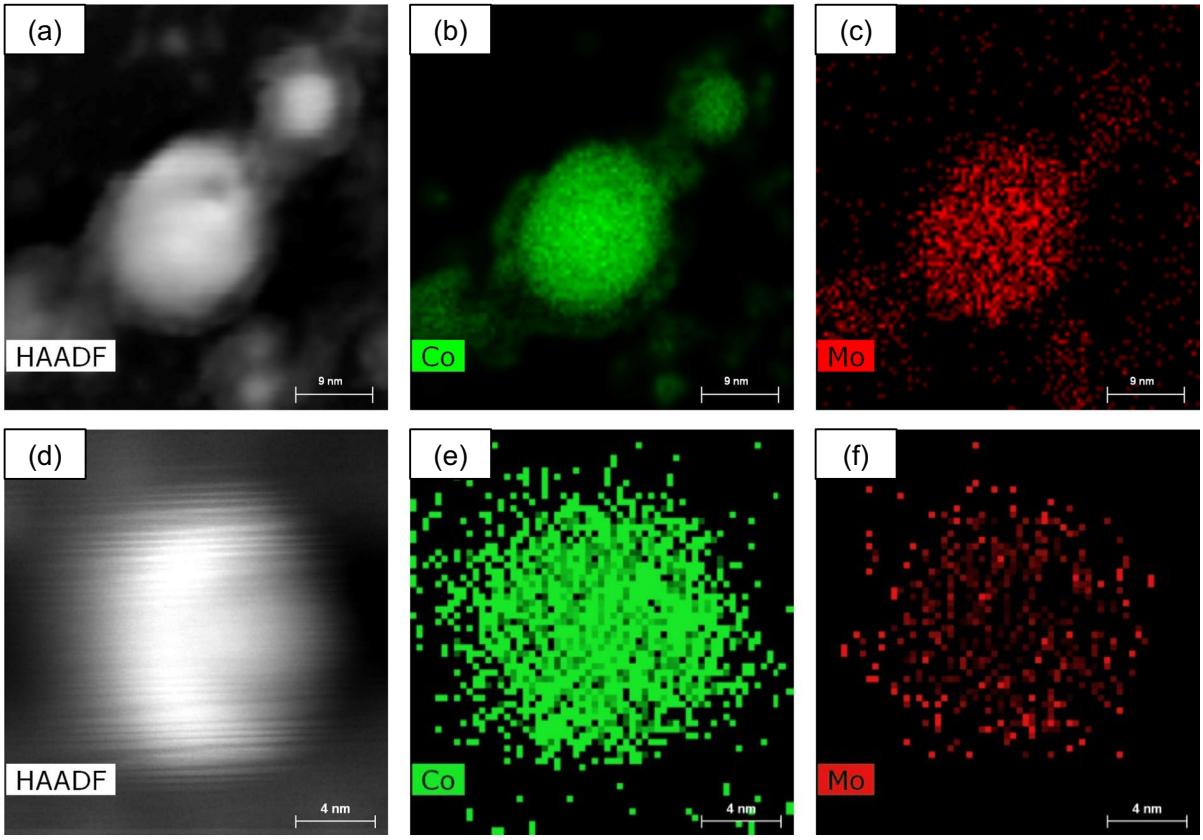

Fig. 3 High-angle annular dark field (HAADF) STEM images of the Co(Mo) nanoparticles showing homogenous mixing of Mo in hcp Co (i.e., no compositional variations within the nanoparticles). A nanoparticle produced with an aperture size of 2.5 mm and sputtering power 100 W is presented in **a**, **b**, **c**. A nanoparticle produced with an aperture size of 7 mm, and sputtering power 50 W is presented in **d**, **e**, **f**

formed with the 7-mm aperture (Fig. 4c), the FFT (Fig. 5d) was again indexed to an hcp structure, in this case the [0111] zone axis, but with slightly different lattice parameters ($a = 2.6$ Å and $c = 4.6$ Å). It is useful to compare these to hcp Co, where $a = 2.504$ Å and $c = 4.07$ Å [20]. The formation of an hcp structure is similar to what was observed in the Co–W system, although in that study, an fcc structure was observed in smaller nanoparticles [16]. Here, no evidence of the fcc structure was observed, even in the smaller nanoparticles. Also, pure Co nanoparticles produced by IGC were predominantly observed to be fcc with some hcp, with the proportion of hcp increasing in larger nanoparticles (in that case, ~ 13 nm) [21].

The lattice parameters observed here can be compared to those for a model hcp Co structure with 18% Mo dissolved into it substitutionally, which would probably enlarge the lattice since Mo is larger than Co. The "*a*" lattice parameter observed here for the nanoparticles is very close to the *a* of the model solid solution structure (2.507 Å). However, the *c* axes of the observed structures are expanded beyond the model structure, by 22% for the nanoparticles formed with a 2.5-mm aperture and 13% for those formed with the 7-mm aperture. The expanded *c* axis could be the result of stacking fault-like defects or self-interstitials along the *c* axis. Mukherjee et al. [15] explained expanded lattices in Fe–Au through a self-interstitial model. Also, the *c* axis-component dislocation loops in hcp Mg introduced stacking faults which expanded the *c* lattice parameter [22], and irradiation-induced vacancies and self-interstitials, again in Mg, were generated and agglomerated preferentially in the basal planes, affecting the *c* axis lattice parameter [22]. Due to the highly energetic IGC process, it

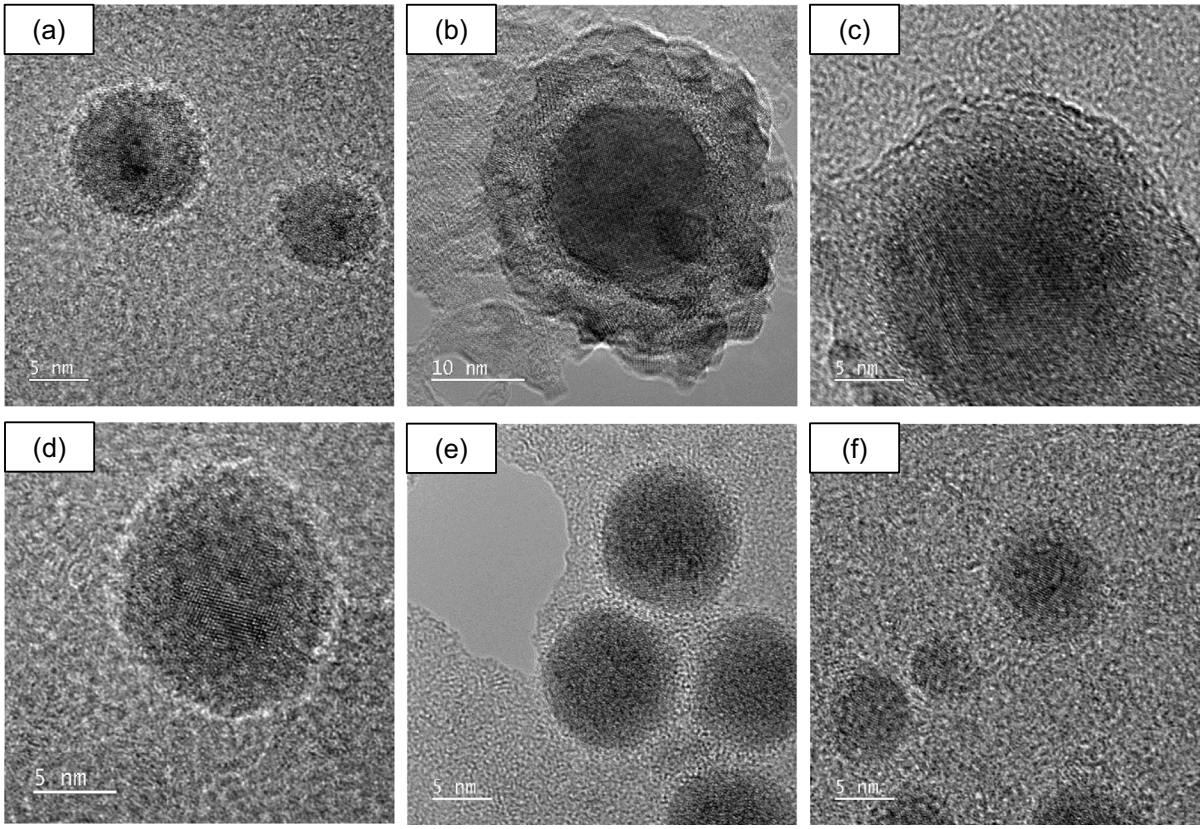

Fig. 4 High-resolution TEM images of the individual as-deposited Co(Mo) nanoparticles produced with varied sputtering power (50 W, 100 W, 150 W) an aperture sizes (2.5, 7 mm). For the 2.5-mm aperture, nanoparticles produced from different powers are presented in **a** 50 W, **b** 100 W, and **c** 150 W. For the 7-mm aperture, nanoparticles produced from different powers are presented in **d** 50 W, **e** 100 W, and **f** 150 W

is reasonable to explain the expansion of the *c* axis by defect formation along this direction. There is some evidence of lattice distortion of the {1101} planes in Fig. 5, suggesting that there is some *c* axis defect structure.

All of the nanoparticles formed under different sputtering powers and aperture sizes displayed ferromagnetic behavior at 300 K, evidenced by hysteretic behavior (Fig. 6). For nanoparticles formed with an aperture size of 2.5 mm, the nanoparticles formed with different sputtering powers have similar coercivities, whereas for nanoparticles formed with a 7-mm aperture, coercivities increased with an increase in sputtering power (Fig. 7). Overall, the coercivities for the nanoparticles produced with a 2.5-mm aperture were significantly higher than the coercivity for the nanoparticles produced with the 7-mm aperture, and also dramatically higher than similar Co–W nanoparticles [16] and pure Co [21].

The difference in coercivity between the nanoparticles formed with the 2.5-mm and 7-mm apertures may be structure-dependent. While the *a* axes are identical, the *c* axis for the nanoparticles produced with the 2.5-mm aperture is expanded compared to the *c* axis of the nanoparticles produced with the 7-mm aperture. An increased *c*/*a* ratio, or increased defect structure along the *c* axis, may lead to an increased magnetocrystalline anisotropy and thus higher coercivity. However, work on Co thin films suggested a decrease in magnetocrystalline anisotropy with increasing *c*/*a* [23]. Further, Bian et al. [24] found that an increase in stacking fault density resulted in a decreased magnetocrystalline anisotropy, although the *c*/*a* ratio in that work was constant. In other systems, an increased aspect (*c*/*a*) ratio did result in an increase in magnetocrystalline anisotropy [25].

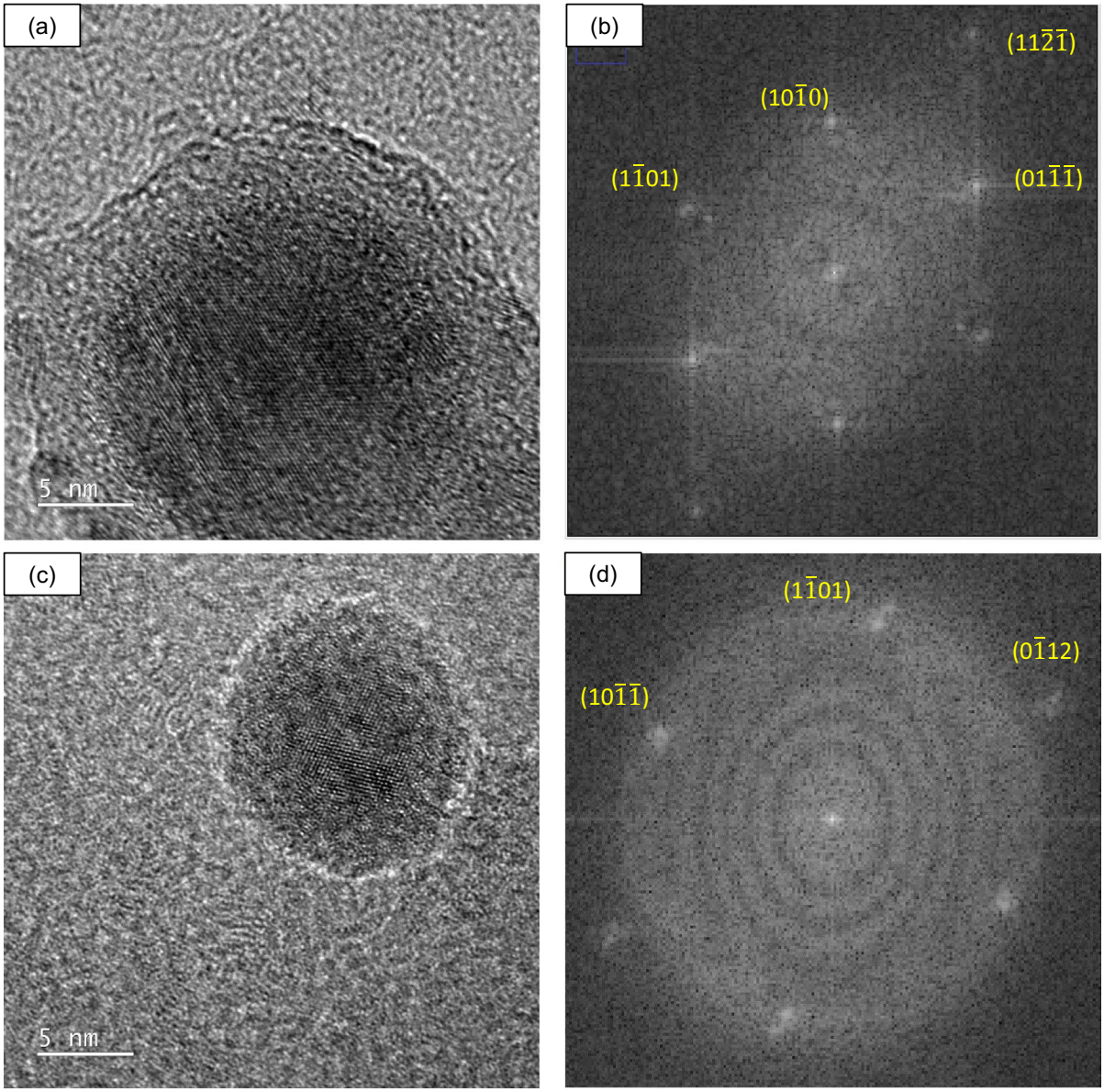

Fig. 5 **a** HRTEM image and **b** indexed FFT of as-deposited Co(Mo) nanoparticle for aperture size of 2.5 mm and 150 W. The FFT indexes to a [1 $\bar{2}$ 1 $\bar{3}$] zone axis for hcp. **c** HRTEM image and **d** indexed FFT of as-deposited Co(Mo) nanoparticle for aperture size of 7 mm and 50 W. The FFT indexes to a [01 $\bar{1}$ 1] zone axis for hcp

The increase in coercivity may also be nanoparticle size–related, as there is a general increase in coercivity as the nanoparticle size decreases (Fig. 8). An increase in coercivity with decreasing scale is reminiscent of behavior of multidomain nanoparticles [26]. However, the single-domain limit for hcp Co is 42 nm [27]; thus, the nanoparticles here are likely in a single-domain state. Hard magnetic materials have been observed to increase in coercivity with decreasing particle/grain size in the single-domain state, absent of any interparticle/intergrain interactions [28]. Further work is necessary to determine the magnetocrystalline anisotropy and further elucidate the size-dependent behavior of the Co(Mo) nanoparticles.

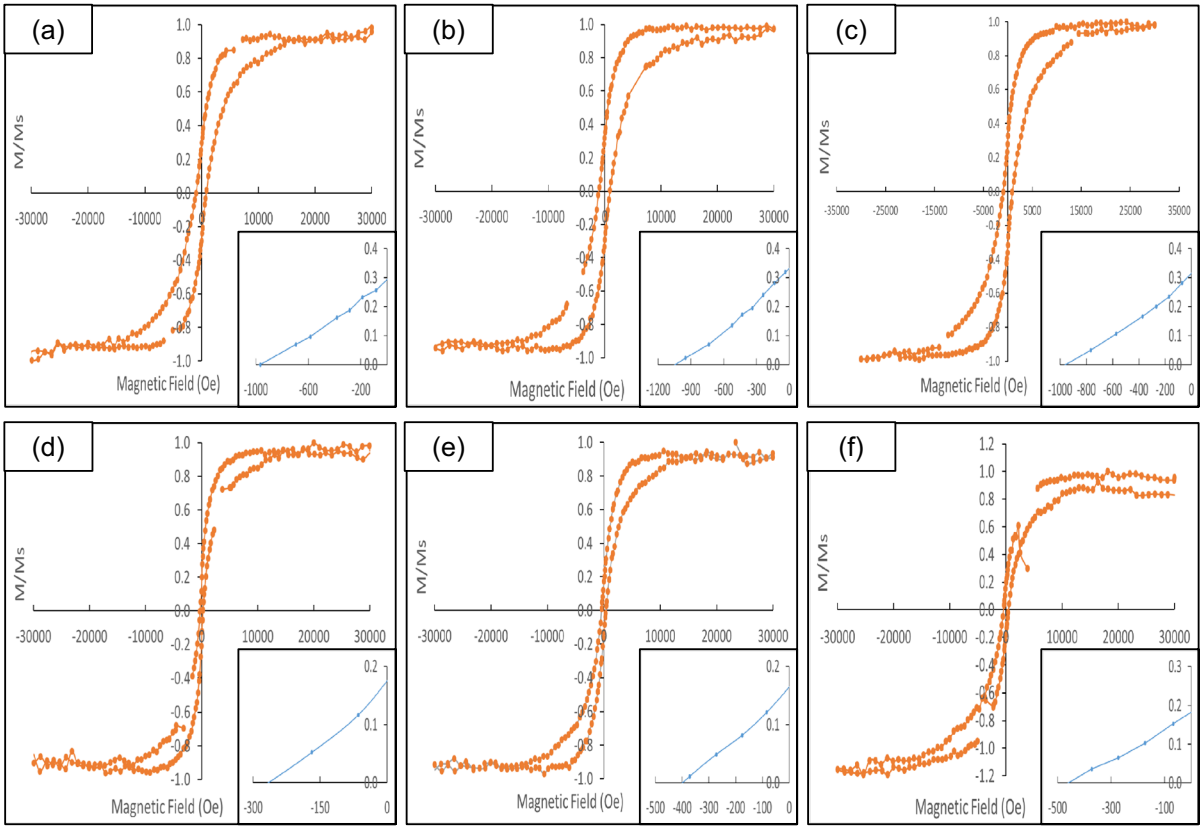

Fig. 6 Hysteresis behavior of as-deposited Co(Mo) nanoparticles produced with varied sputtering power (50 W, 100 W, 150 W) and aperture sizes (2.5, 7 mm) measured at 300 K. The inset shows second quadrant behavior. **a–c** Hysteresis curves for nanoparticles formed with the 2.5-mm aperture at 50, 100, and 150 W, respectively. **d–f** Hysteresis curves for nanoparticles formed with the 7-mm aperture at 50, 100, and 150 W, respectively

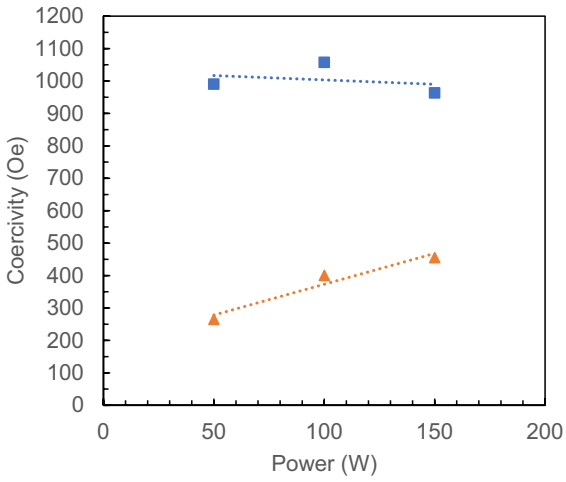

Fig. 7 Coercivity as a function of sputtering power for Co(Mo) nanoparticles produced with aperture sizes of 2.5 mm (squares) and 7 mm (triangles) measured at 300 K

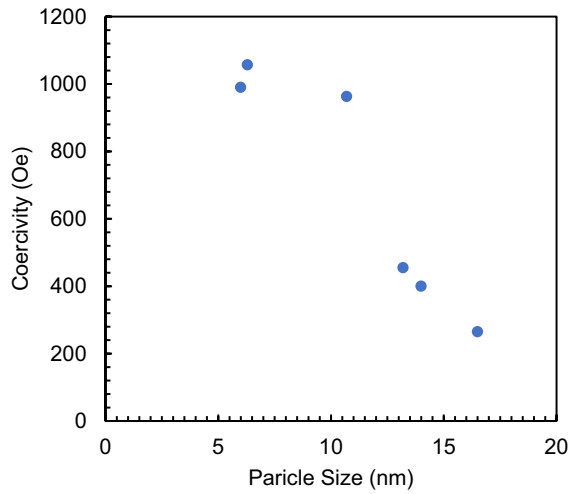

Fig. 8 Coercivity as a function of nanoparticle size

Conclusions

Inert gas condensation was used to generate Co–Mo nanoparticles with significant extension of the solid solubility. The nanoparticles were found to have an hcp structure and chemically homogeneous—i.e., complete dissolving of Mo in Co. While the equilibrium solubility of Mo in hcp Co is ~ 1 atomic percent, here, it was determined that ~ 18 at% Mo was dissolved into the hcp Co structure. Nanoparticle size was found to be slightly related to sputtering power and more strongly related to aperture size (which controls dwell time in the nucleation chamber, but can alter dynamics).

The Co(Mo) solid solution nanoparticles were observed to be ferromagnetic. The coercivity values were strongly related to whether the nanoparticles were formed with the 2.5- or 7-mm aperture, with the smaller aperture producing higher coercivities, and a small dependence on sputtering power. However, the coercivity may be more related to nanoparticle size.

Author Contribution S.D—Data Curation, Investigation, Methodology, Writing- original draft, review & editing J.S—Conceptualization, Funding acquisition, Investigation, Project administration, Supervising, Writing- review & editing.

Funding This work was supported by NSF Division of Materials Research, Directorate for Mathematics & Physical Sciences under the award number DMR 2211872. The research was performed in part in the Nebraska Nanoscale Facility: National Nanotechnology Coordinated Infrastructure by the National Science Foundation under award no. ECCS: 2025298, and with support from the Nebraska Research Initiative through the Nebraska Center for Materials and Nanoscience and the Nanoengineering Research Core Facility at the University of Nebraska-Lincoln.

Data Availability No datasets were generated or analysed during the current study.

Declarations

Competing interests The authors declare no competing interests.

References

1. Gutfleisch O, Willard MA, Brück E, Chen CH, Sankar SG, Liu JP (2011) Magnetic materials and devices for the 21st century: stronger, lighter, and more energy. Adv Mater 23:821–842. https://doi.org/10.1002/adma.201002180
2. Magnetic materials market size, share & trends analysis report by type (hard/permanent, semi-hard, soft), by application (automotive & transportation), by region, and segment forecasts, Market Analysis Report, 2022 – 2030. https://www.grandviewresearch.com/industry-analysis/magnetic-materials-market-analysis-market. Accessed 21 Dec 2023
3. Kramer MJ, McCallum RW, Anderson IA, Constantinides S (2012) Prospects for non-rare earth permanent magnets for traction motors and generators. JOM 64:752–763. https://doi.org/10.1007/s11837-012-0351-z
4. Cui J, Kramer M, Zhou L, Liu F, Gabay A, Hadjipanayis G, Balasubramanian B, Sellmyer D (2018) Current progress and future challenges in rare-earth-free permanent magnets. Acta Mater 158:118–137. https://doi.org/10.1016/j.actamat.2018.07.049
5. Skomski R, Sharma V, Balamurugan B, Shield J E, Kashyap A, and Sellmyer D J, Anisotropy of doped transition-metal magnets Proc. REPM'10, Eds.: S. Kobe and P. McGuinness, Jozef Stefan Institute, Ljubljana, p. 55–60, (2010).
6. Kashyap A, Manchanda P, Sahota PK, Skomski R, Shield JE, Sellmyer DJ (2011) Anisotropy of W in Fe and Co". IEEE Trans Magn 47(10):3336–3339
7. Boettinger WJ, Coriell SR, Sekerka RF (1984) Mechanisms of microsegregation-free solidification. Mater Sci Eng 65:27. https://doi.org/10.1016/0025-5416(84)90196-4
8. Ferrando R, Jellinek J, Johnson RL (2008) Nanoalloys: from theory to .applications of alloy clusters and nanoparticles. Chem Rev 108:845. https://doi.org/10.1021/cr040090g
9. Sharif MJ, Yamazoe S, Tsukuda T (2014) Selective hydrogenation of 4-nitrobenzaldehyde to 4-aminobenzaldehyde by colloidal RhCu bimetallic nanoparticles. Top Catal 57:1049–1053. https://doi.org/10.1007/s11244-014-0269-5
10. Zhang Q, Kusada K, Wu D, Ogiwara N, Yamamota T, Toriyama T, Matsumura S, Kawaguchi S, Kubota Y, Honma T, Kitagawa H (2019) Solid solution alloy nanoparticles of a combination of immiscible Au and Ru with a large gap of reduction potential and their enhanced oxygen evolution reaction performance. Chem Sci 10:5133. https://doi.org/10.1039/C9SC00496C

11. Zlotea C, Morfin F, Nhuyen TS, Nelayah J, Ricolleau C, Latroche M, Piccolo L (2014) Nano-alloying bulk-immiscible iridium and palladium inhibits hydride formation and promotes catalytic performances. Nanoscale 6:9955. https://doi.org/10.1039/C4NR02836H
12. Kusada K, Yamauchi M, Kobayashi H, Kitagawa H, Kubota Y (2010) Hydrogen-storage properties of solid-solution alloys of immiscible neighboring elements with Pd. J Am Chem Soc 132:15896. https://doi.org/10.1021/ja107362z
13 Haberland H, Karrais M, Mall M, Thurner Y (1992) Thin films from energetic cluster impact: a feasibility study. J Vac Sci Technol A Vacuum Surfaces, Film 10:3266. https://doi.org/10.1116/1.577853
14. Ren Z, Xie Z, Ming R, Zhan Y, Xin Y, Han J, Zhuang L, Liu Y, Zhu Y (2023) Overcoming the problem of insolubility to controllably synthesize AuCo alloy as a high performance electrocatalyst for the oxygen reduction reaction. New J Chem 47(46):21150–21154. https://doi.org/10.1039/D3NJ04055K
15 Mukherjee P, Zhou L, Kramer MJ, Shield JE (2013) Formation of non-equilibrium Fe-Au solid solutions in nanoclusters. Appl Phys Lett 102:243103. https://doi.org/10.1063/1.4811412
16. Golkar F, Kramer MJ, Zhang Y, Skomski R, Sellmyer DJ, Shield JE (2013) Solubility extension and phase formation in gas-condensed Co-W nanoclusters. J Nanopart Res 15:1638. https://doi.org/10.1007/s11051-013-1638-x
17. Golkar F (2015) Inert-gas condensed Co-W nanoclusters: formation, structure and magnetic properties. Dissertation, University of Nebraska-Lincoln.
18. Chapman B (1980) Glow discharge processes: sputtering and plasma etching. Wiley, New York
19. Koten MA, Mukherjee P, Shield JE (2015) Core-shell nanoparticles driven by surface energy differences in the Co-Ag, W-Fe and Mo-Co systems. Part Part Syst Charact 32:848–853. https://doi.org/10.1002/ppsc.201500019
20. Cullity BD, Stock SR (2001) Elements of X-ray diffraction, 3rd edn. Prentice Hall, Upper Saddle River
21 Yamamuro S, Sumiyama K, Konno TJ, Suzuki K (1999) Structural and magnetic evolution in self-assembling process of nanometer-sized Co clusters. Mater Trans JIM 40(12):1450–1455. https://doi.org/10.2320/matertrans1989.40.1450
22. Xu W, Zhang Y, Cheng G, Mathaudhu SN, Scattergood RO, Koch CC, Lavernia EJ, Zhu Y (2017) On the origin and behavior of irradiation-induced c-component dislocation loops in magnesium. Acta Materialia 131:457–466. https://doi.org/10.1016/j.actamat.2017.04.015
23 Wang JJ, Sakurai T, Oikawa K, Ishida K, Kikuchi N, Okamota S, Sato H, Shimatsu T, O. (2009) Kitakami, Magnetic anisotropy of epitaxially grown Co and its alloy thin films. J Phys Condens Matter 21:185008. https://doi.org/10.1088/0953-8984/21/18/185008
24. Bian B, Yang W, Laughlin DE, Lambeth DN (2001) Stacking faults and their effect on magnetocrystalline anisotropy in Co and Co-alloy thin films. IEEE Trans Magn 37:1456. https://doi.org/10.1109/20.950869
25. Shima H, Oikawa K, Fujita A, Fukamichi K, Ishida K, Sakuma A (2004) Lattice axial ratio and large uniaxial magnetocrystalline anisotropy in L10-type FePd single crystals prepared under compressive stress. Phys Rev B 70:224408. https://doi.org/10.1103/PhysRevB.70.224408
26. He X, Zhong W, Au C-T, Du Y (2013) Size dependence of the magnetic properties of Ni nanoparticles prepared by thermal decomposition method. Nano Res lett 8:446. https://doi.org/10.1186/2F1556-276X-8-446
27. Skomski R, Nanomagnetics (2003) J. Phys.: Condens. Matter 15:R841https://doi.org/10.1088/0953-8984/15/20/202
28. Akdogan N, Hadjinpanayis GD, Sellmyer DJ (2009) Anisotropic Sm-(Co, Fe) nanoparticles by surfactant—assisted ball milling. J Appl Phys 105:07A710. https://doi.org/10.1063/1.3067851